Quantitative studies on inner interfaces in conical metal joints using hard X-ray inline phase contrast radiography

S. Zabler[1)], T. Rack[2)], A. Rack[3)], K. Nelson[2)]

1) Technical University of Berlin – Institute for Materials Science, EB 13, Strasse des 17. Juni 135, D-10623 Berlin, Germany

2) Charité University Medicine – Clinic for Oral and Maxifacial Surgery, Augustenburger Platz 1, D-13353 Berlin, Germany

3) European Synchrotron Radiation Facility, 6 rue Jules Horowitz, BP 220, F-38043 Grenoble, France

Abstract

Quantitative investigation of micrometer and sub-micrometer gaps between joining metal surfaces is applied to conical plug-socket connections in dental titanium implants. Microgaps of widths well beyond the resolving power of industrial X-ray systems are imaged by synchrotron phase contrast radiography. Furthermore, by using an analytical model for the relatively simple sample geometry and applying it to numerical forward simulations of the optical Fresnel-propagation we show that quantitative measurements of the microgap width down to 0.1 µm is possible. Image data recorded at the BAM*line* (BESSY-II light source, Germany) are presented, with the resolving power of the imaging system being 4 µm in absorption- and ~14 µm in phase contrast mode (z_2 = 0.74 m). Thus, phase contrast radiography combined with numerical forward simulations is capable of measuring the widths of gaps which are two orders of magnitude thinner than the conventional detection limit.

Keywords: X-ray phase contrast, X-ray imaging, microgap, conical joints, dental implants, titanium, Fresnel propagation, non-destructive evaulation, numerical simulations.

I. Introduction

Industrial radiography which is suited to probe the internal structure of mm- to cm-sized metallic components does usually not have the sufficient spatial resolution to detect micrometer- and sub-micrometer gaps and misfits at connecting interfaces. Unlike industrial X-ray tubes, the unique properties of hard X-ray synchrotron light sources, namely high brilliance and partial coherence, allow for the direct imaging of (sub-)micrometer voids and cracks even in highly X-ray attenuating objects [1,2]. People have been using synchrotron light sources for high-resolution X-ray imaging experiments since the 1980s [3]. Later during the 1990s edge enhancement methods were added – known as inline X-ray phase contrast – which detects smallest interfaces and features both in high- and low-density materials [4, 5, 6].

Despite its excellent detection efficiency, inline X-ray phase contrast imaging is generally known as a qualitative measurement technique. By employing optical Fresnel-propagation, very small structural features (inclusions and interfaces) which are well beyond the conventional resolving power of the imaging system can be detected in terms of interference fringes [7]. Yet, these fringes only indicate the position of the feature while its precise shape and size remain unknown. From the general outline of the interferences, light inclusions and voids - both showing an X-ray focusing effect - can be separated from dense and / or high-Z inclusions which show a diffusive effect. Zabler et al. have demonstrated that phase contrast tomography of microtubules within human dentin, a structure which comprises both voids and dense mineral sheaths embedded in a collagen-rich matrix, require numerical forward simulations of the optical Fresnel-propagation in order to interpret the interference signals [8]. Consequently, unless the sample structure is well known, a precise estimate of density, atomic number Z or refractive index n from phase contrast X-ray images is not feasible. Phase-retrieval procedures are partially able to solve this problem by numerically reversing the Fresnel propagation [9, 10]. Yet, interferences originating from interfaces between two materials of strongly different refractive indices (e.g., air – steel) represent a problem for these methods since phase retrieval procedures are commonly based on the assumption of either a weak or a smooth transition of n from one material to the next [11]. Furthermore, low pass filtering is often required reducing further the resolving power and obscuring small details [12]. Obviously, for this reason interfaces and inclusions which are of sub-resolution size and / or buried in highly X-ray attenuating metal components, cannot be phase-retrieved from Fresnel-propagated radiographs.

With this paper we present a new approach which compares phase contrast radiography to numerical simulations of the optical Fresnel-propagation through a known sample structure in order to measure the width of inner microgaps between connecting metal components. Such simulations have already been used as basis for the quantitative exploration of polychromatic phase contrast X-

ray images to study micropipes in SiC wafers [13]. In order to simulate the phase contrast of such microscopic features *a priori* knowledge about the sample geometry and material is required which makes this approach impractical for complex structures and / or multiphase materials. Nevertheless, there is a large number of industrial applications concerning air-metal interfaces in devices of relatively simple geometric design for which the quantitative measurement of micrometer and sub-micrometer voids and gaps is both feasible and required [14].

As a model system for this study the conical joint in metallic tooth replacements was chosen: These dental implant devices are widely used in dentistry (~ 1 million implantations per year in Germany). They are commonly made of titanium, according to a four component design which comprises: 1) the implant-body (acting as socket), which is screwed into the mandibular or maxillary bone, 2) the abutment (plug), which connects to the implant-body and – after successful osseointegration of the latter – supports the 3) crown, and 4) the abutment-screw which tightens the first two components [15]. Omitting crown and abutment-screw, this design is commonly referred to as two-piece implant. The focus of our study is to measure the width of micrograps at the conical implant-abutment connection (IAC) *in situ* under load. Micrometer and sub-micrometer misfits in such metallic connections are an inevitable consequence of limited machine precision. It is known that particularly for small millimeter-sized plug-and-socket connections the tolerance on shape and roughness of the joining surfaces has a critical influence on the fatigue limit under cyclic load [16, 17, 18].

Until recently, microgaps in two-piece dental implants were only considered for horizontal IACs (so called butt-joint connections) [19, 20]. Using high-resolution synchrotron-based radiography, we have proven the existence of microgaps at the IAC interface of dental implants which have a conical connection [21]. In this paper we will introduce how *a priori* information on the sample material and the very simple geometric design can be used for numerical forward-simulations of the optical Fresnel-propagation in order to infer interference fringes observed in phase contrast radiographs of conical IACs to the actual width of the microgap at the connecting interface. In combination with newly developed X-ray sources of increasing brilliance, a later stage of development of this method which will not require synchrotron light is theoretically possible [22, 23]. Obviously, this could stimulate further industrial applications.

II. Materials and method

A. Inline phase contrast X-ray imaging

Unlike conventional X-ray imaging techniques which are based on laboratory sources (electrons

impinging onto metallic bulk or thin transmission targets which then emit a broad polychromatic spectrum of X-rays), X-ray beams which originate from a synchrotron source are highly brilliant, *i.e.* they have an extremely low angular divergence and a very high spectral photon flux density (photons/ mm²/ s/ 0.1%BW). Consequently, synchrotron light can be monochromatized (for hard X-rays, this is commonly done by reflection on single crystals or multilayer mirrors) and, most importantly, the emitted wave front at the position of the experiment disposes of a partial spatial coherence which is due to the long distances between source and sample (up to several 100 m) [14]. This partial coherence allows for recording interference-fringes in defocused X-ray images. In order to switch from conventional X-ray imaging (of the linear sample attenuation) to inline X-ray phase contrast imaging, the distance between detector and sample has to increase from a few millimeters up to several tens of centimeters (therefore the sample-detector distance is commonly referred to as propagation-distance) – depending on the coherence properties of the beam [12,24]. Furthermore, the phase contrast images have to be recorded at high spatial resolution (few micrometers and less) to capture the small-spaced fringes. Edge enhancement allows for detecting objects and /or discontinuities which are smaller than the resolution limit of the imaging system [4]. This is possible because size and amplitude of the fringe patterns increase with longer propagation distances. For recording the high-resolution X-ray images a scintillator screen is used which converts the X-rays into a visible light image. The latter is commonly magnified by high-quality microscope lenses and projected onto a low-noise CCD camera. A mirror in the optical path allows for positioning the CCD perpendicular to- and thus protect it from the X-rays (similar to a periscope). Typical resolutions achieved with these systems range from several tens of micrometers down to the (sub-)micrometer range, depending on the thickness of the scintillator screen, the wavelength of its light emission and the microscope lenses' numerical aperture [1]. Figure 1 shows in a drawing how microgaps at the IAC can be visualized by phase contrast radiography.

B. Numerical Fresnel-propagation

The design of many dental implants is relatively simple comprising a conical IAC with rotational symmetry. Therefore, an analytical model (detailed in the appendix) was created in order to simulate the X-ray phase contrast originating from a microgap at such IACs. These simulations require parametrization of the X-ray beam which was adjusted to match the settings of experiments performed at the BAM*line* station (BESSY-II light source, Helmholtz center Berlin, Germany): photon energy: 50 keV, detector point spread function: 4.0 µm, source-to-sample distance z_1 = 35 m, sample-to-detector (propagation-)distance z_2 = 0.005 ...0.8 m [21]. A relatively large Gaussian X-ray source size of 0.65 mm (as deduced from fitting phase contrast profiles of large microgaps whose

widths were determined from absorption radiographs, see results section) was assumed, although a smaller value (0.16 mm) has been reported from Talbot measurements using 18 keV X-rays on the same beamline [25]. Our assumption is based on the fact that in this paper numerical simulations are compared to radiographs that have been measured in the so-called single-bunch mode of the BESSY-II storage ring which results in the larger source size. Phase contrast images which were taken at z_2 = 0.74 m sample-detector distance will be reported in the results section. These images are blurred by the demagnified light source which can be calculated as $0.65 \cdot z_2/z_1 = 0.01374$. As a consequence the effective resolving power is reduced to ~14 µm whereas the resolution in contact (absorption, meaning $z_2 \sim 0$ m) images is only limited by the detector's point spread function (~4 µm). At synchrotron beamlines X-ray propagation is quasi-parallel, thus the transmitted wave $u_0(x)$ behind the sample ($z = 0$) is described by multiplication of the incoming wave $u_{inc}(x)$ with the complex transmission function $T(x)$. For reasons of simplicity, we will only consider a line intensity profile across the IAC, thus x designs the coordinate perpendicular to the interface (see appendix):

$$u_0(x) = u_{inc}(x) \cdot T(x) \qquad (1)$$

$$T(x) = \exp\left(i\phi(x) - B(x)\right) \qquad (2).$$

With $B(x)$ the absorption and $\phi(x)$ the associated phase shift. Both B and ϕ are calculated as the line integrals along the direction of X-ray propagation (z) of the imaginary and the real part respectively of the complex refractive index n. Values of n were defined for each material component c according to the relation $n_c = 1 - \delta_c + i\beta_c$. The standard implant material is commercially pure (cp) titanium of grade 4 (density 4.51 g/cm^3, according to ASTM F-67) whereas the abutment is commonly made of the titanium alloy Ti-6Al-4V ELI (= Extra Low Interstitial, referring to the extra low oxygen content) with density 4.43 g/cm^3 (ASTM F-136). Thus, both line integrals in (1) can be written as sums:

$$\phi(x) = \phi_0 - \frac{2\pi}{\lambda}\left(\delta_{imp} \cdot t_{imp}(x) + \delta_{abt} \cdot t_{abt}(x)\right) \qquad (3)$$

$$B(x) = \frac{2\pi}{\lambda}\left(\beta_{imp} \cdot t_{imp}(x) + \beta_{abt} \cdot t_{abt}(x)\right) \qquad (4)$$

with $t_{imp}(x)$ and $t_{abt}(x)$ the total thickness of implant- and abutment material, respectively (the exact model is detailed in the appendix). ϕ_0 corresponds to a constant phase shift through vacuum ($n = 1$) and is neglected since it has no influence on the outcome of the simulations. The refractive indices for 50 keV X-rays of the implant and the abutment material are n_{imp} = 1 – 3.44e-7 + i 8.64e-10 and n_{abt} = 1 – 3.39e-7 + i 8.21e-10, respectively (calculated with the ESRF software XOP [26]). Propagating the transmitted wave $u_0(x)$ means convolution with the Fresnel-propagator $P_D(x)$:

$$u_D(x) = u_0(x) * P_D(x) \qquad (5)$$

$$P_D(x) = \frac{1}{i\lambda D}\exp\left(i\pi\frac{x^2}{\lambda D}\right) \qquad (6).$$

Hereby D denotes the effective propagation distance: $D = z_1 \cdot z_2 / (z_1 + z_2)$, z_1 the source-to-sample- and z_2 the sample-to-detector distance. For convenience the transmitted wave $u_0(x)$ is first Fourier transformed and then multiplied with $\hat{p}_D(f) = \exp(-i\pi\lambda D f^2)$ - the propagator in Fourier-space with f the *spatial frequency*, conjugate variable to x - then back-transformed to real-space where the intensity is calculated as the square modulus of the propagated $u_D(x)$ wave:

$$I_D(x) = |u_D(x)|^2 \qquad (7).$$

Convolution of $I_D(x)$ with the detector point-spread function and the demagnified source size is again performed in Fourier space. In analogy to absorption radiography, where intensity maps are converted to linear attenuation values by calculating $\mu.t = -\ln(I/I_0)$, with I_0 being the 'flatfield' image which normalizes I for the inhomogeneous beam intensity, we will present measurements and simulation results in terms of the negative logarithm of the normalized propagated intensity $I_D(x)$ referring to this value as the "linear signal". For the simulations $I_0 = 1$ is assumed. All calculations are done with the program GNU Octave © [27].

III. Results

In order to measure the widths of microgaps in conical IACs an implant of relatively simple cylindrical design was used (ANKYLOS, DENTSPLY Friadent GmbH, Mannheim Germany). This design is described by the analytical geometrical model detailed in the appendix. An extra-axial force of 200 N was applied in 30° inclination resulting in a one-sided opening of the microgap towards the top of the conical IAC while implant and abutment join tightly at the bottom. This approach is schematized in Fig. 2a. Five line profiles - from the bottom to the top - were extracted from a high-resolution contact image (z_2 ~ 40 mm) of the loaded implant (b). Before calculating the line profiles, first the image region showing the gap was cropped and rotated by 5.7° in order to visualize the gap in vertical direction. Line profiles were then extracted at equidistant positions corresponding to vertical steps of 0.4 mm. In order to improve the signal-to-noise ratio a line-width of 86 µm (200 pixels of ~ 0.43 µm size) was used to calculate averaged profiles of 0.4 mm length (ImageJ ® software package). From Fig. 2b one can clearly see the gap width increasing from the bottom to the top whereby gap widths for the first three profiles can be estimated from the lateral extension of the discontinuity in the line profiles (as schematized Fig. 2b). The widths of the corresponding microgaps were thus estimated to 20.5 µm, 13.0 µm and 7.0 µm. The smaller gaps are only visible as a discontinuity in the absorption profile hence a width estimation is not feasible.

Figure 3 shows the absorption profiles of the three smallest gaps from Fig. 2b along with the corresponding phase contrast profiles. For measuring these profiles the same sample was imaged under identical conditions, only the propagation distance was increased from $z_2 \sim 40$ mm to $z_2 = 740$ mm. All microgaps are now highlighted by a strong edge-enhancement effect which is characterized by a pronounced bright-dark fringe-pair. For the 7.0 µm gap this edge-enhancement mainly amplifies the interface signal by a factor of 4. Most importantly, the smallest two gaps are now well visible as bright interference lobes. Estimating their width is now possible by comparing the bright interferences to numerical forward simulations. In order to parametrize these simulations we first modeled the interferences of the phase contrast of larger gaps (20.5 µm, 13 µm and 7 µm) whose widths have already been determined from the absorption profiles (cf. Fig. 2b). Based on the resulting set of consistent parameters (image resolution, source size, etc.) a width of 2.2 µm and 0.2 µm was estimated for the smallest gaps (these values yield the best match between measurement and simulation). Note that despite identical camera and line profile settings the phase contrast profiles appear jagged in contrast to the corresponding absorption profiles. This is probably due to the fact that by means of the inline phase contrasting not only the micrograp but all other inhomogeneities and phase boundaries inside the sample and the surface roughness are emphasized as well.

In order to evaluate the error margin of this result, simulations of slightly smaller and slightly larger gaps are compared to the 'best fits'. Figure 4a shows the phase-enhanced profile of the smallest (0.2 µm) gap along with three numerical simulations corresponding to 0.1 µm (half), 0.2 µm (best fit) and 0.4 µm (double) wide gaps. The choice of 0.2 µm gap-width was mainly made by manually adjusting the height and width of the bright signal to the measured data. Simulations corresponding to half and double the gap width can clearly be identified as under- and overestimation of the true gap width. Yet, simulations of a 0.3 µm and a 0.15 µm gap appear too similar to be distinguished as 'better' and 'worse', which is why we stipulate a maximum uncertainty of +/- 100 % for the gap width. As can be seen in Fig. 4b, this margin also applies when fitting the dark-bright fringe-pair of the 2.2 µm gap which is compared to simulations of 1.1 µm, 2.2 µm and 4.4 µm gaps. Cross-checking over all comparisons of the larger gaps' phase contrast line profiles (7 µm, 13 µm and 22 µm – as measured from the absorption profiles) with numerical forward simulations we found a constant confidence margin of approx. +/- 2 µm.

In order to find the optimal propagation distance and to exploit the methods sensitivity, we further considered the sample-detector distance z_2 as well as the gap width as free parameters. Figure 5a shows a 3D surface plot: the linear signal is plotted as a function of z_2 – which varies between 0 and 0.8 m – and of the coordinate x across the microgap whose width is set to 0.2 µm. The x-range corresponds to a profile of 0.13 mm length. From Fig. 5 we can see that the fringes peak-to-peak

signal, in other words the visibility of the gap gains in intensity when z_2 is increased from 0 to ~200 mm. The fringe-contrast remains mainly dark-bright which can be explained by considering the microgap acting as a refractive lens thus focusing the light from the outer implant side into the gap (because $Real(n_{imp}) < Real(n_{air})$). At z_2 ~ 200 mm the peak-to-peak value is maximum whereas for propagation distances z_2 > 200 mm it decreases because the fringes are blurred out increasingly by convolution with the demagnified X-ray source size. Despite this z_2-dependant blurring of the interferences the microgap remains well visible, even at z_2 = 800 mm. Three representative line-profiles are depicted in Fig. 5b, calculated for the 0.2 µm gap and for z_2 = 4 mm, 200 mm and 800 mm. In accordance with the measurements (Fig. 2b) the microgap is hardly noticeable in the absorption profile whereas it is well visible for the larger propagation distances, outlined by strong interference fringes. Note that the profile at z_2 = 200 mm is visibly sharper whereby the dark and bright fringes are more pronounced compared to the profile calculated for z_2 = 800 mm.

The simulated Fresnel-propagation for a large microgap (20 µm width) as a function of distance z_2 ranging from 0 to 0.8 m is shown in the 3D surface plot in Fig. 6a. Similar to Fig. 5a, three representative line profiles are depicted for the large gap in Fig. 6b for z_2 = 4 mm (absorption), 200 mm and 800 mm (phase contrast). In contrast to the 0.2 µm gap, a significant drop / discontinuity in the linear absorption signal $I(z_2 = 4$ mm) is observed which matches our observations from Fig. 2. Phase contrast (200 mm and 800 mm profiles in Fig. 6b) is found to enhance the visibility of the gap but a less trivial fringe pattern is observed at z_2 = 200 mm (not one but two minima follow the first sharp bright maximum). Fresnel-propagation over z_2 =800 mm propagation distance yields a single bright-dark fringe-pair whereby we note that compared to the 0.2 µm gap (cf. Fig. 5), the fringe-contrast is now inversed (bright-dark instead of dark-bright).

A third surface plot is shown in Fig. 7 calculated for a constant propagation distance z_2 = 740 mm and a variable gap width ranging from 0.05 µm to 30 µm (this range was chosen to fit the measured gap widths in Fig. 2). The peak-to-peak contrast (difference between interference maximum and minimum) increases monotonously, until - for gaps larger than ~ 20 µm - the dark interference minimum splits into a double lobe.

IV. Discussion

We have demonstrated that by combining X-ray phase contrast microradiography with numerical forward simulations of the optical Fresnel-propagation the width of sub-resolution inner microgaps can be analyzed quantitatively and we have applied this method to internal conical joints of dental implants made of titanium. The simple geometric design of these implants allows the use of an analytical model for the Fresnel-contrast originating from microgaps at the IAC interface. For

example the Ankylos Friadent implant which features a conical plug-socket connection was chosen. *A priori* knowledge about sample material and geometry was used to infer the interference fringes observed in phase contrast radiographs of the microgap directly to the actual gap width. Particularly for gaps smaller than the detector resolution (< 4 µm), matching between modeled and measured line profiles across the gap proved to be very effective for estimating its width (cf. Fig. 4). Remaining uncertainties about the linear signal (either absorption- or inline phase contrast) possibly resulting from incoherent light scattering, image noise and / or imaging artifacts (e.g., deviation from ideal sample geometry, scratches on the top of or reflections inside the scintillator screen) give rise to a relatively large confidence margin for the gap width of +/- 100 %. For gaps larger than 2 µm we observed this margin to approach a constant value of +/- 2 µm. Considering that the peak widths and amplitudes depend on many parameters (energy bandwidth, X-ray source size, angle of the gap with respect to the implant axis, vertical position of the line profile, etc.) the results - indicating that the true gap width is not less than half and not more than twice of the 'best fit' - can be considered a reasonably good error margin. Clearly, direct access to the gap width via absorption imaging is favored, yet only possible for gaps which are sufficiently large compared to the resolving power of the imaging system. Additionally the microgap's extension parallel to the X-ray beam, i.e. tangential to the IAC interface has to be sufficiently large to create a noticeable discontinuity in the absorption signal. On the other hand we have shown that combining phase contrast radiography with forward simulations of the latter allows for quantitative measurements of micro- and sub-micrometer gaps. Requirements on the resolving power and on the signal-to-noise ratio are thereby far less compared to absorption imaging due to the spatial extension of the interference fringes. Extrapolating from Fig. 7 the detection and measurement limits for inner microgaps should at least extend down to 0.1 µm, whereby analysis of the measured line profiles indicates that the true image resolution at z_2 = 740 mm is ~ 14 µm (cf. Fig. 4b). Thus, microgaps which are two orders of magnitude smaller than the conventional detection limit can be analyzed.

For measurements performed with the BESSY-II synchrotron light source operating in the so-called 'single bunch mode', our simulations indicate further that by using smaller propagation distances z_2 in the range of 200 to 400 mm interferences would be more pronounced although fringe patterns recorded at these distances can be more complicated than a single pair of dark and bright fringes (cf. Fig. 6b). Note that despite the good fit of the dark and bright fringes with the forward simulations (cf. Fig. 4) the overall amplitude of the simulated signal had to be augmented by 35 – 40 % in order to match the measurement. This correction can be explained by light reflections between the two faces of the scintillator screen which cause an artificially bright flatfield image. By normalizing the intensity of the radiographs with the latter the X-ray linear signal is thus over-estimated. Also, our simulations assume a gap of constant width over the total conical interface whereas in reality

implant and abutment touch each other at discrete contact points. Hence the gap width is not constant over the IAC interface. Consequently the gap is probably more localized than what is assumed by our simulations.

It is desirable to record phase contrast radiographs of mechanically loaded implants in order to study the opening of microgaps at the IAC interface. Loading involves fixating the implant in a mechanical device which prevents the user from taking full tomographic scans of the IAC. Yet, in the near future we hope to overcome this limitation and extend our studies of the IAC to in-situ microtomography, thus providing a three-dimensional measurement of microgaps in conical joints.

Acknowledgements
We thank Dr. H. Riesemeier and R. Britzke for support during beamtime at BESSY. Our gratitude goes to Dr. W. Semper for sample preparation and helpful discussion.

Appendix - Geometrical model for simulating microgaps at the IAC by X-ray propagation

Figure 8 shows a 3D scheme of the analytical model of the IAC used for this work. Interference fringes are evaluated at the measurement point *P* marked by the red dot. An oblique cut is drawn through the implant whereby the intersecting plane (with the coordinates *x* and *y*) is normal to the IAC interface at *P* (i.e. the cut is oblique with an angle ϕ). In the original coordinate system at *P*, the outer radius of the cylindrical implant is r_2 and the outer radius of the conical abutment is r_1 ($r_1 < r_2$). Because the linear signal is only evaluated near *P* (-0.2 mm < *x* < 0.2 mm with *x* = 0 at *P*) the radius of the inner abutment screw is of no importance for the simulation and is therefore omitted in the calculation. The birds view onto the cutting plane is shown in Fig. 9: Implant and abutment are characterized by ellipses. Note that the ellipsoidal cut through the conical IAC has a different centre compared to the cut through the implant socket. This centre-shift Δx can be calculated by considering the horizontal distance *R* between *P* and the opposite intersecting point along the *x*-axis, which is equal to the short (*y*-) axis *b* of the abutment ellipse

$$R = b = \frac{r_1}{1 - \tan^2 \phi} \qquad \text{(A1)}$$

a and *b* denote the long and the short axis of the abutment ellipse, whereas *A* and *B* correspond to the long and short axis of the implant ellipse. Using eq. A1, the long axis *a* of the abutment ellipse in the (*x*, *y*) plane is found as

$$a = \frac{R}{\cos\phi} = \frac{r_1}{(1 - \tan^2 \phi)\cos\phi} \qquad \text{(A2)}$$

and the *x*-shift of the abutment versus the implant ellipses' centres (cf. Fig. 9):

$$\Delta x = R - r_1 = \frac{r_1 \tan^2 \phi}{1 - \tan^2 \phi} \qquad \text{(A3).}$$

Concerning the implant ellipse, the short axis eqals $B = r_2$ whereas the long axis is

$$A = \frac{r_2}{\cos \phi} \qquad \text{(A4).}$$

For the simulation we assumed parallel X-ray transmission along the *y*-axis. Therefore the intensity is calculated as a function of *x* with the origin $x = 0$ on the inner side of the implant. The thickness projection along *y* for the implant material (typically CP titanium grade-4) is thus:

$$t_{imp} = \sqrt{B^2 - (x + \Delta x - a - g)^2 \frac{B^2}{A^2}} \quad \text{for } x \le 0 \qquad \text{(A5)} \qquad \text{and}$$

$$t_{imp} = \sqrt{B^2 - (x + \Delta x - a - g)^2 \frac{B^2}{A^2}} - \sqrt{(b+g)^2 - (x - g - a)^2 \frac{(b+g)^2}{(a+g)^2}} \quad \text{for } x > 0 \qquad \text{(A6).}$$

whereby *g* is the width of the microgap. For $x > g$ we have to add the thickness projection of the abutment material (typically Ti-6Al-4V ELI alloy) which is

$$t_{abt} = \sqrt{b^2 - (x - a - g)^2 \frac{b^2}{a^2}} \qquad \text{(A7).}$$

Eqs. (A5)-(A7) are inserted into eqs. (3) and (4) in order to calculate the projections of the real and the imaginary parts of the materials refractive indices n at the microgap. According to the Ankylos implant design, we used the values $\phi = 5.7°$, $r_2 = 1.75$ mm, $r_1 = 1.05$ ..1.42 mm and $g = 0.2$ ..20 µm.

Figure captions:

Fig. 1: Schematic representation of radioscopic microgap of the implant abutment connection. The entire tooth replacement is composed of implant (I), abutment (A), crown (C) and abutment screw (S). As sketched, due to the partial spatial coherence of the X-ray beam, the small microgap at the implant-abutment joint (IA) is highlighted by interferences appearing as a dark-bright line contrast in the radiographic image.

Fig. 2: a) Schematic illustration of microgap measurements under extra-axial load (30° with respect to the main implant axis) for a conical IAC (Ankylos Friadent, Mannheim, Germany). b) Five line profiles of 0.4 mm length each (A-E) were derived from a high-resolution absorption radiograph

using a line-width of 200 pixels for averaging. To assure that the gap is open towards the upper left part of the IAC, 200 N force were applied to the abutment while taking the radiograph.

Fig. 3: Comparison of three measured line profiles corresponding to the smallest gaps. Red dashed lines: absorption profiles (cf. Fig. 2b), blue solid lines: phase contrast profiles taken at the same position but with a propagation distance of 740 mm. The three sets of line profiles are shifted along the x –axis to avoid overlap.

Fig. 4: a) Comparison of the measured phase contrast line profile (grey spheres) at z_2 = 740 mm with the numerical forward propagation (simulation) of the presumably 0.2 µm wide gap (blue solid line). For error estimation simulations for 0.1 µm (red dashed line) and 0.4 µm (green dotted line) wide microgaps are shown alongside the 'best fit'. b) Measured phase contrast line profile for the 2.2 µm wide gap (grey solid circles) together with the corresponding numerical fit (blue solid line). Again for error estimation simulations of 1.1 (green dotted line) µm and 4.4 µm (red dashed line) wide microgaps are shown alongside the 'best fit'.

Fig. 5 a) 3D surface plot of phase contrast (in terms of linear signal) forming at a 0.2 µm wide microgap at the IAC interface. Propagation distances range from 0 to 0.8 m. b) Three simulated line profiles of 0.2 mm length across the IAC are shown for a 0.2 µm wide microgap: At z_2 = 4 mm the signal results mostly from attenuation whereas at z_2 = 200 mm and 800 mm interference fringes appear due to Fresnel-propagation. The relatively large effective source size (0.65 mm) which has been assumed for the simulations causes strong signal blurring particularly at z_2 = 800 mm.

Fig. 6 a) 3D surface plot of the phase contrast (in terms of linear signal) forming at a 20 µm wide gap at the IAC interface. Propagation distances range from 0 to 0.8 m. b) Three simulated line profiles of 0.2 mm length across the IAC are shown for a 20 µm wide gap: The absorption contrast at z_2 = 4 mm shows a visible discontinuity at the joint whereas the fringes at z_2 = 200 mm feature dark and bright lobes. The phase contrast at z_2 = 800 mm shows a broad bright-dark fringe contrast.

Fig. 7 3D surface plot of the phase contrast formation of a microgap of variable width ranging from 0.05 µm to 30 µm, calculated at the IAC for a constant propagation distance z_2 = 740 mm.

Fig. 8 3D schematic view of the geometric model of the IAC. *P* designates the measurement point, *x* and *y* the coordinates of the intersecting plane (conical angle ϕ) which is perpendicular to the IAC interface at point *P*.

Fig. 9 Birds view onto the intersecting plane of the geometric IAC model. The yellow ring corresponds to the abutment material, *g* designs the width of the microgap. The abutment screw is indicated by the central ellipse but not accounted for in the calculation since only a very short *x*-profile around the IAC is simulated.

References

1. A. Koch, C. Raven, P. Spanne, A. Snigirev: J. Opt. Soc. Am. A **15**, 1940 (1998).
2. S. Zabler, A. Rack, I. Manke, K. Thermann, J. Tiedemann, N. Hartnill, H. Riesemeier: J. Struct. Geol. **30**, 876 (2008).
3. J.H. Kinney, Q.C. Johnson, U. Bonse, R. Nusshardt, M.C. Nichols: The performance of CCD array detectors for application in high-resolution tomography, in: D.K. Bowen and L.V. Knight (eds), Proceedings of SPIE. X-ray imaging II **691**, 43 (1986).
4. T.J. Davis, D. Gao, T.E. Gureyev, A.W. Stevenson, S.W. Wilkins: Nature **373**, 595 (1995).
5. P. Cloetens, R. Barrett, J. Baruchel, J…P. Guigay, M. Schlenker: J. Phys. D: Appl. Phys. **29**, 133 (1996).
6. A. Momose: Opt. Express **11**, 2303 (2003).
7. A. Snigirev, I. Snigireva, V. Kohn, S. Kuznetsov, I. Schelokov: Rev. Sci. Instrum. **66**, 5486 (1995).
8. S. Zabler, H. Riesemeier, P. Fratzl, P. Zaslansky: Opt. Express **14**, 8584 (2006).
9. P. Cloetens, W. Ludwig, J. Baruchel, D. van Dyck, J. van Landuyt, J.-P. Guigay, M. Schlenker: Appl. Phys. Lett. **75**, 2912 (1999).
10. K.A. Nugent, T.E. Gureyev, D.F. Cookson, D. Paganin, Z. Barnea: J. Appl. Phys. **81**, 110 (1997).
11. J.-P. Guigay: Optik **49**, 121 (1977).
12. S. Zabler, P. Cloetens, J.-P. Guigay, J. Baruchel, M. Schlenker: Rev. Sci. Instrum. **76**, 0737051 (2005).
13. V. Kohn, T.S. Argunova, J.H. Je: Appl. Phys. Lett. **91**, 171901 (2007).
14. J. Banhart (ed): Advanced Tomographic Methods in Materials Research and Engineering (Oxford University Press 2008).
15. J. R. Davis (ed): Handbook of Materials for Medical Devices (ASM International, Materials Park, OH 44073-0002 2003).
16. L. Steinebrunner, S. Wolfart, K. Ludwig, M. Kern: Clin. Oral Impl. Res. **19**, 1276 (2008).
17. S.A. Hoyer, C.M. Stanford, S. Buranadham, T. Fridrich, J. Wagner, D. Gratton: J. Prosth. Dent. **85**, 599 (2001).
18. A. Khraisat, R. Stegaroiu, S. Nomura, O. Miyakawa: J. Prosth. Dent. **88**, 604 (2002).
19. T. Tsuge, Y. Hagiwara, H. Matsumura: Dental Materials Journal **27**, 29 (2008).
20. D. Byrne, F. Houston, R. Cleary, N. Claffey: J. Prosth. Dent. **80**, 184 (1998).
21. A. Rack, T. Rack, M. Stiller, H. Riesemeier, S. Zabler, K. Nelson: J. Synchrotron Radiat. **17**, 289 (2010).
22. T. Tuohimaa, M. Otendal, H.M. Hertz: Appl. Phys. Lett. **91**, 074104 (2007).
23. S.W. Wilkins, T.E. Gureyev, D. Gao, A. Pogany, A.W. Stevenson: Nature **384**, 335 (1996).
24. J.-P. Guigay, S. Zabler, P. Cloetens, C. David, R. Mokso, M. Schlenker: J. Synchrotron Radiat. **11**, 476 (2004).
25. A. Rack, S. Zabler, B.R. Müller, H. Riesemeier, G. Weidemann, A. Lange, J. Goebbels, M. Hentschel, W. Görner: Nucl. Instrum. Methods Phys. Res., Sect. A **586**, 327 (2008).
26. M.S. del Rio, R.J. Dejus: XOP: recent developments, in: A.T. Macrander, A.K. Freund, T. Ishikawa and D.M. Mills (eds), Proceedings SPIE. Crystal and Multilayer Optics **3448**, 340 (1998).
27. University of Wisconsin: Octave Homepage, http://www.octave.org.

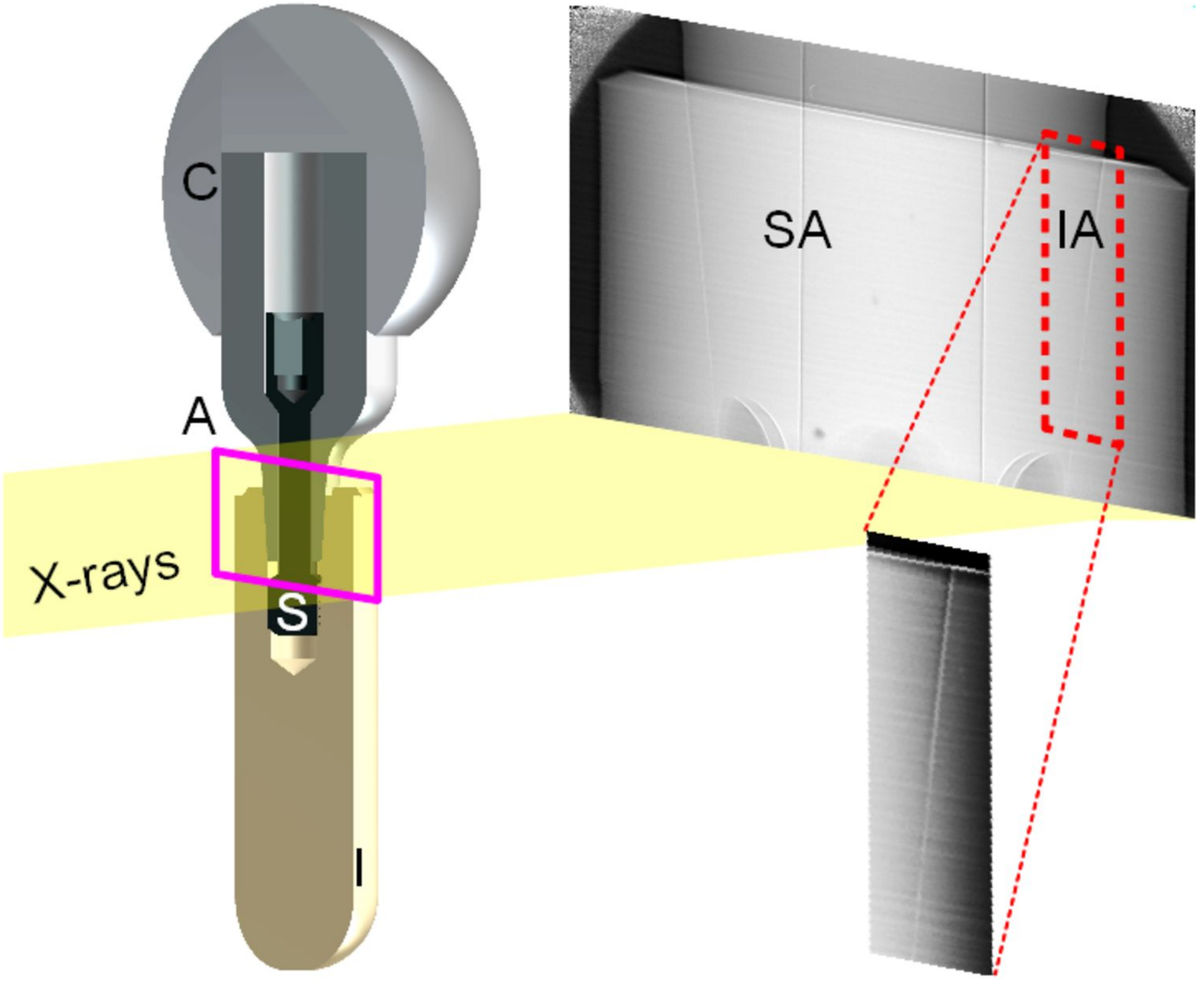
C
A
X-rays
S
I
SA
IA

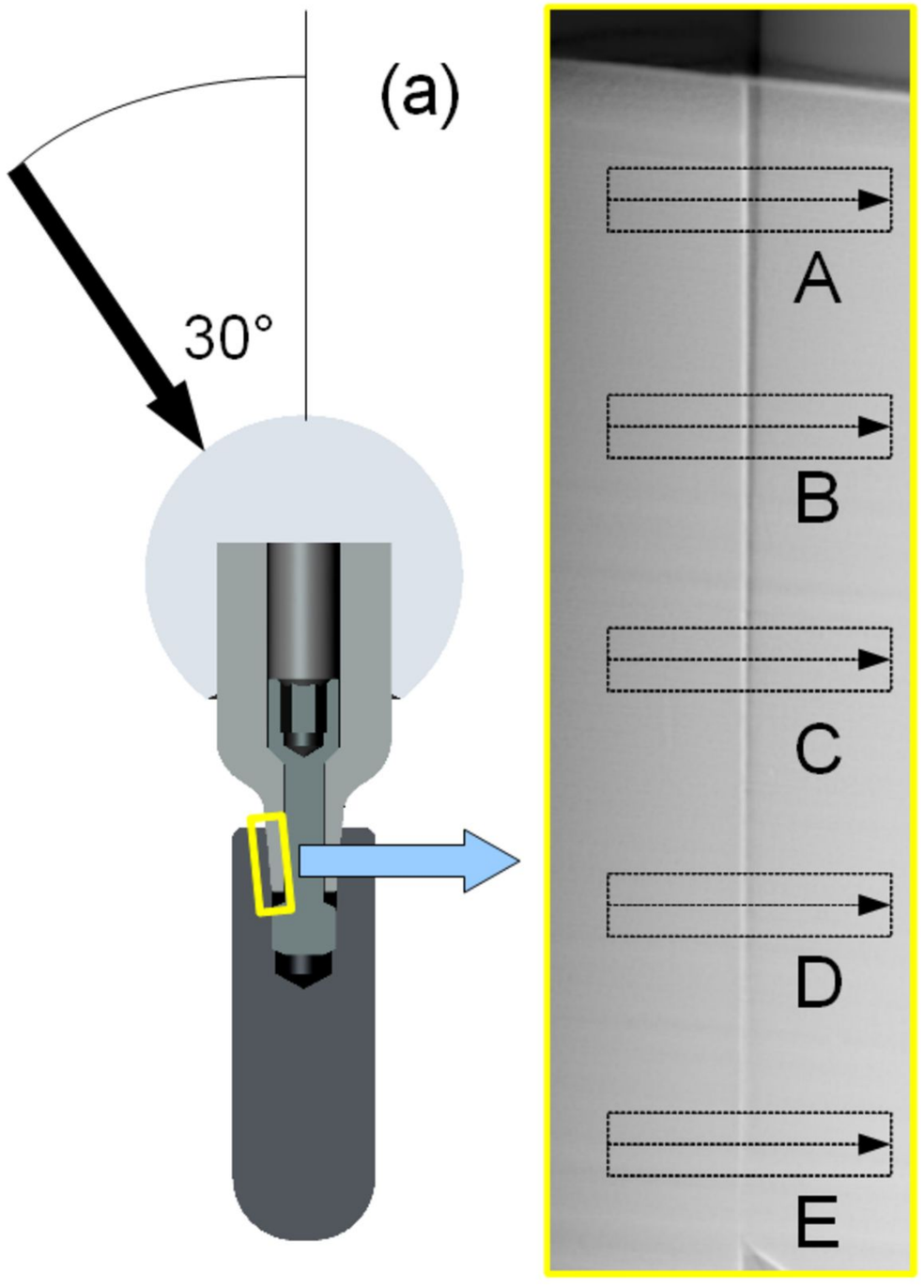
(a)
30°
A
B
C
D
E

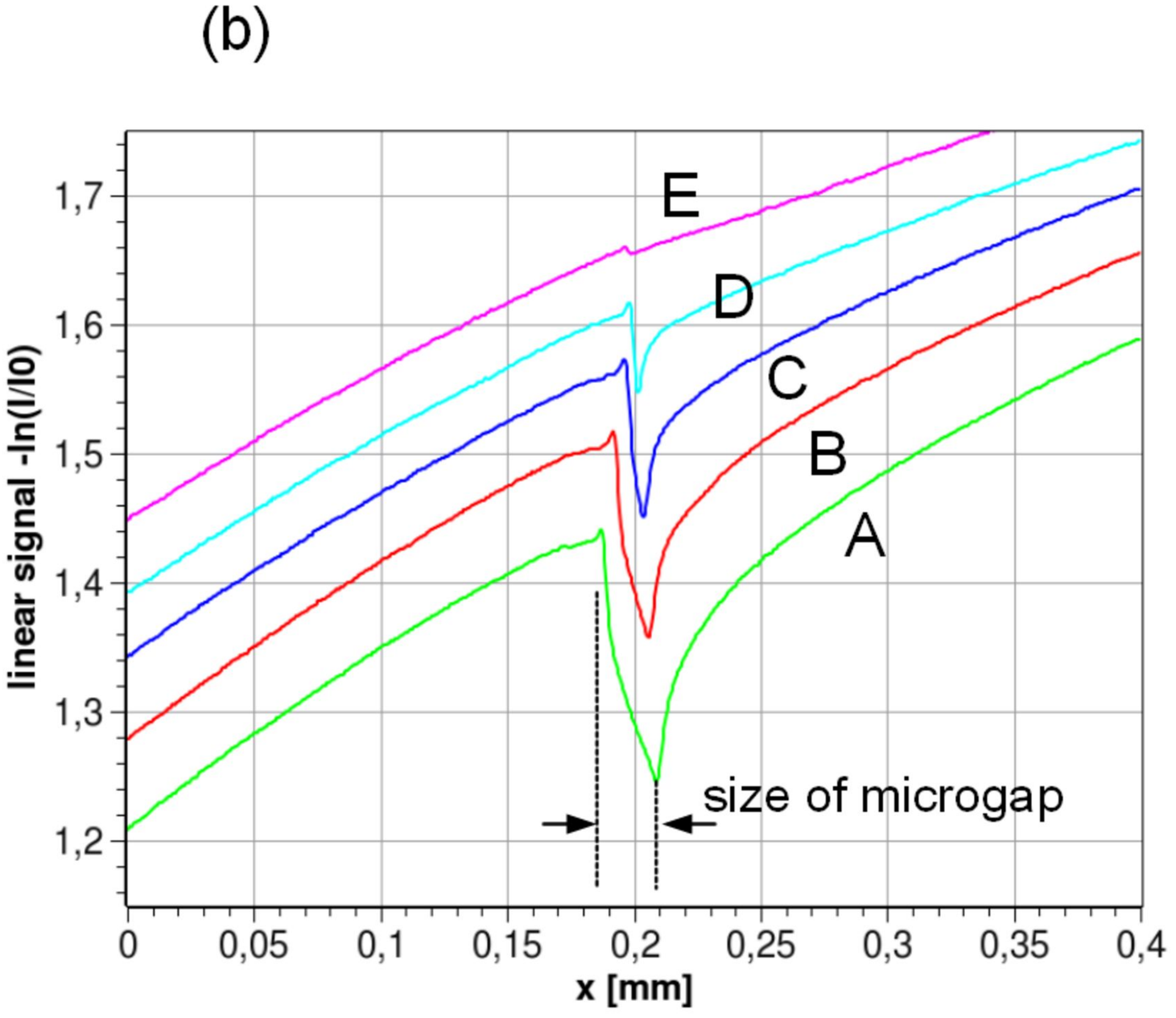
(b)
linear signal -ln(I/I0)
1,7
1,6
1,5
1,4
1,3
1,2
0
0,05
0,1
0,15
0,2
0,25
0,3
0,35
0,4
x [mm]
E
D
C
B
A
size of microgap

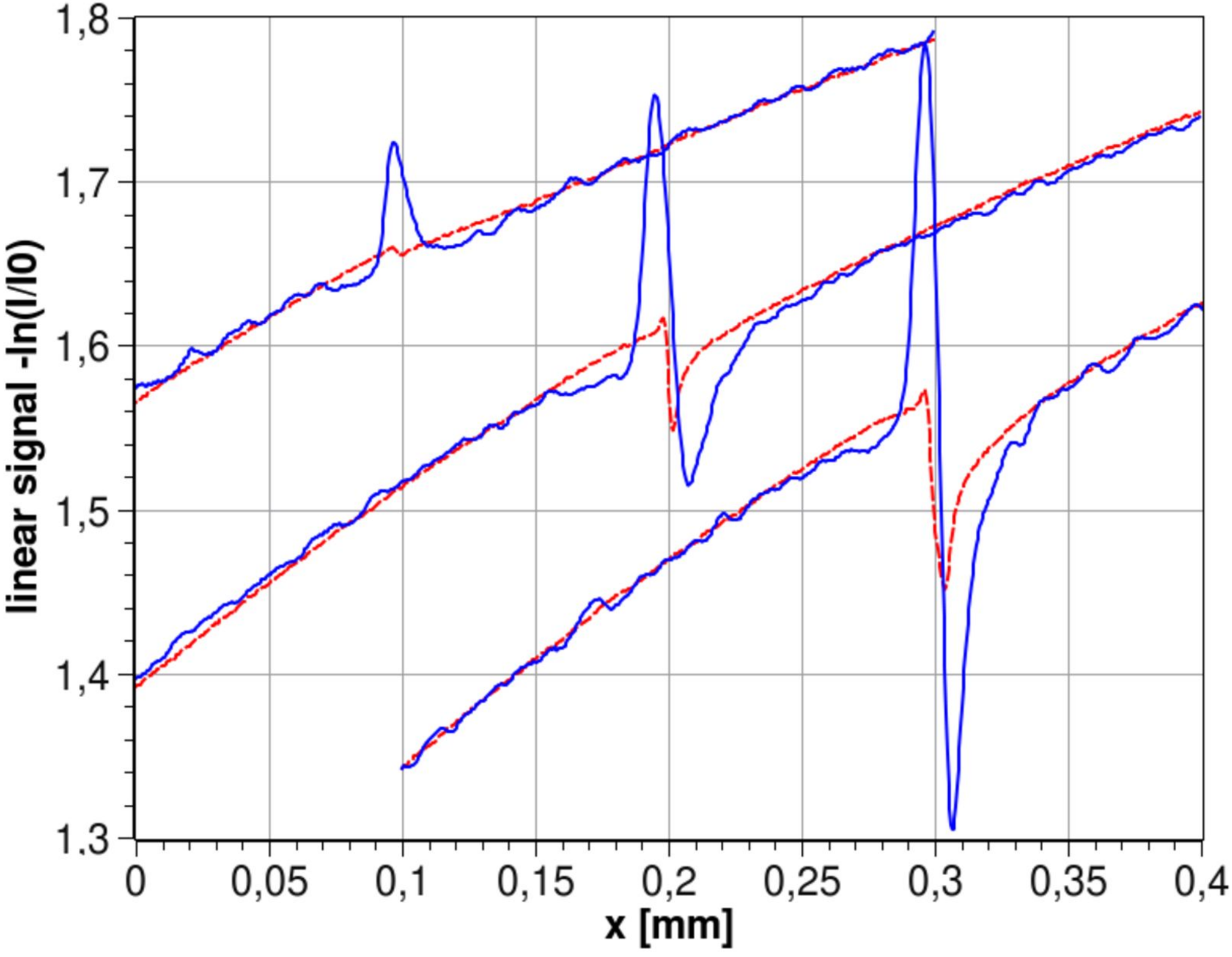
1,8
1,7
1,6
1,5
1,4
1,3
linear signal -ln(I/I0)
0
0,05
0,1
0,15
0,2
0,25
0,3
0,35
0,4
x [mm]

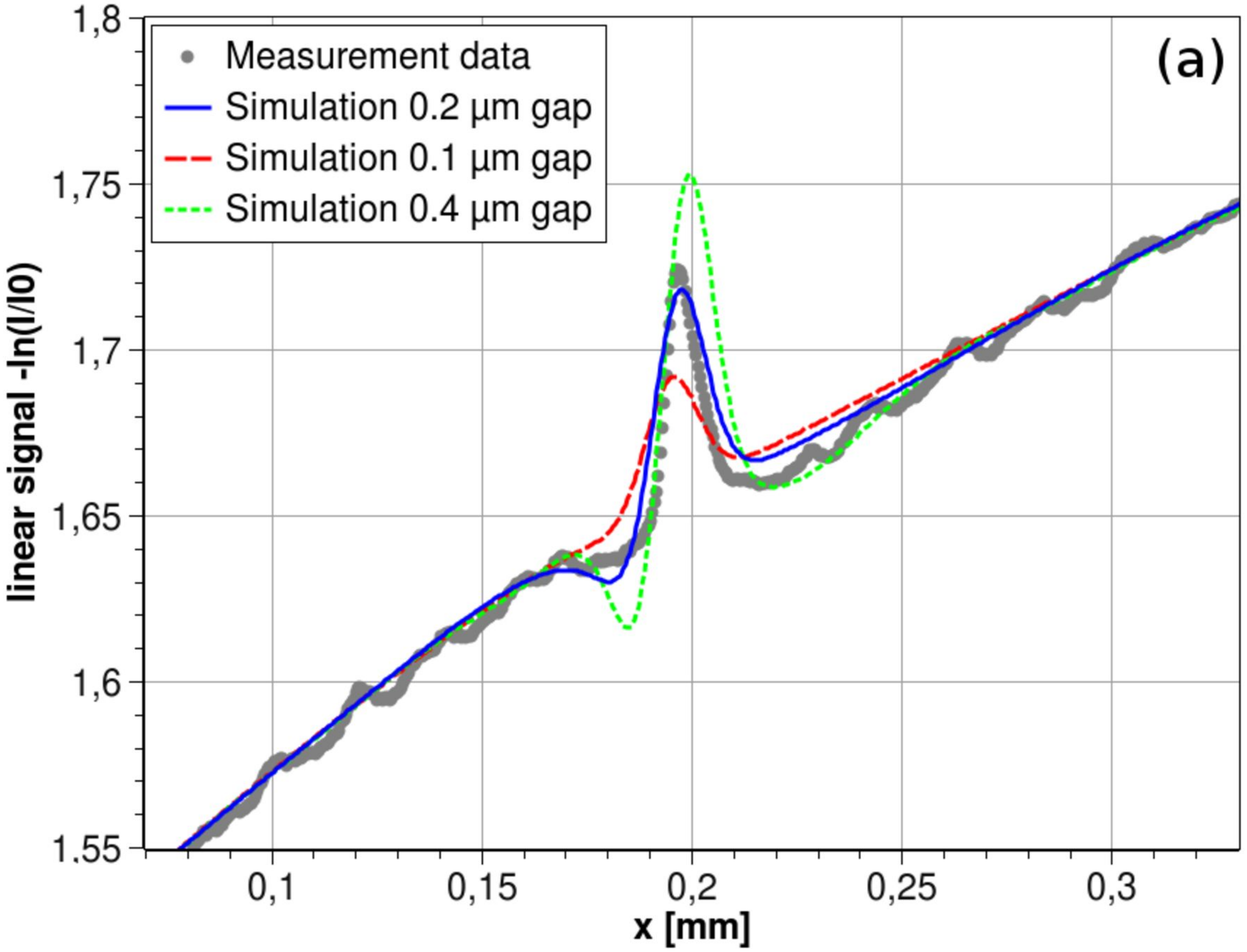
Measurement data
Simulation 0.2 µm gap
Simulation 0.1 µm gap
Simulation 0.4 µm gap
(a)
linear signal -ln(I/I0)
1,8
1,75
1,7
1,65
1,6
1.55
0,1
0,15
0,2
0,25
0,3
x [mm]

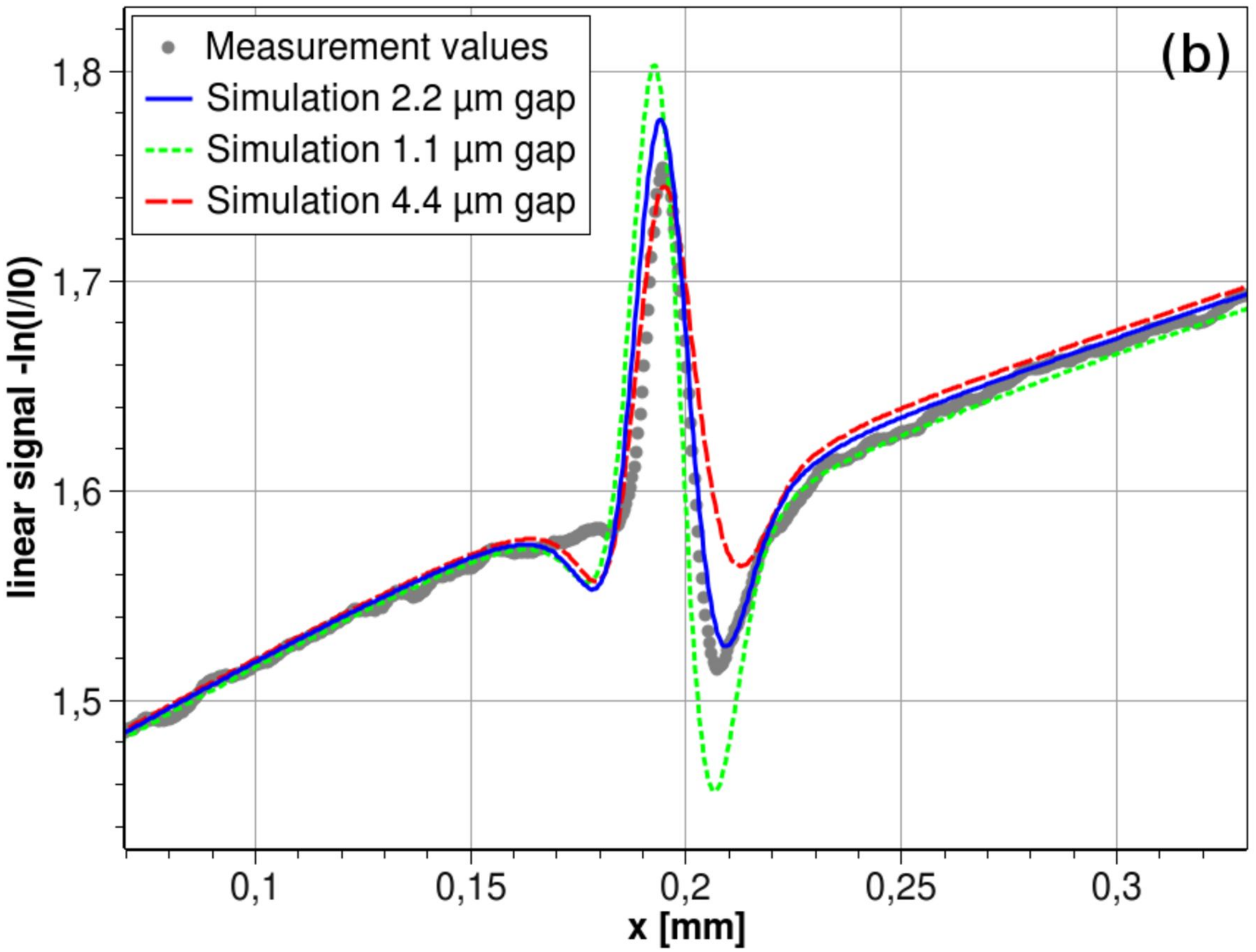
Measurement values
Simulation 2.2 µm gap
Simulation 1.1 µm gap
Simulation 4.4 µm gap
(b)
linear signal -ln(I/I0)
1,8
1,7
1,6
1,5
0,1
0,15
0,2
0,25
0,3
x [mm]

(a)

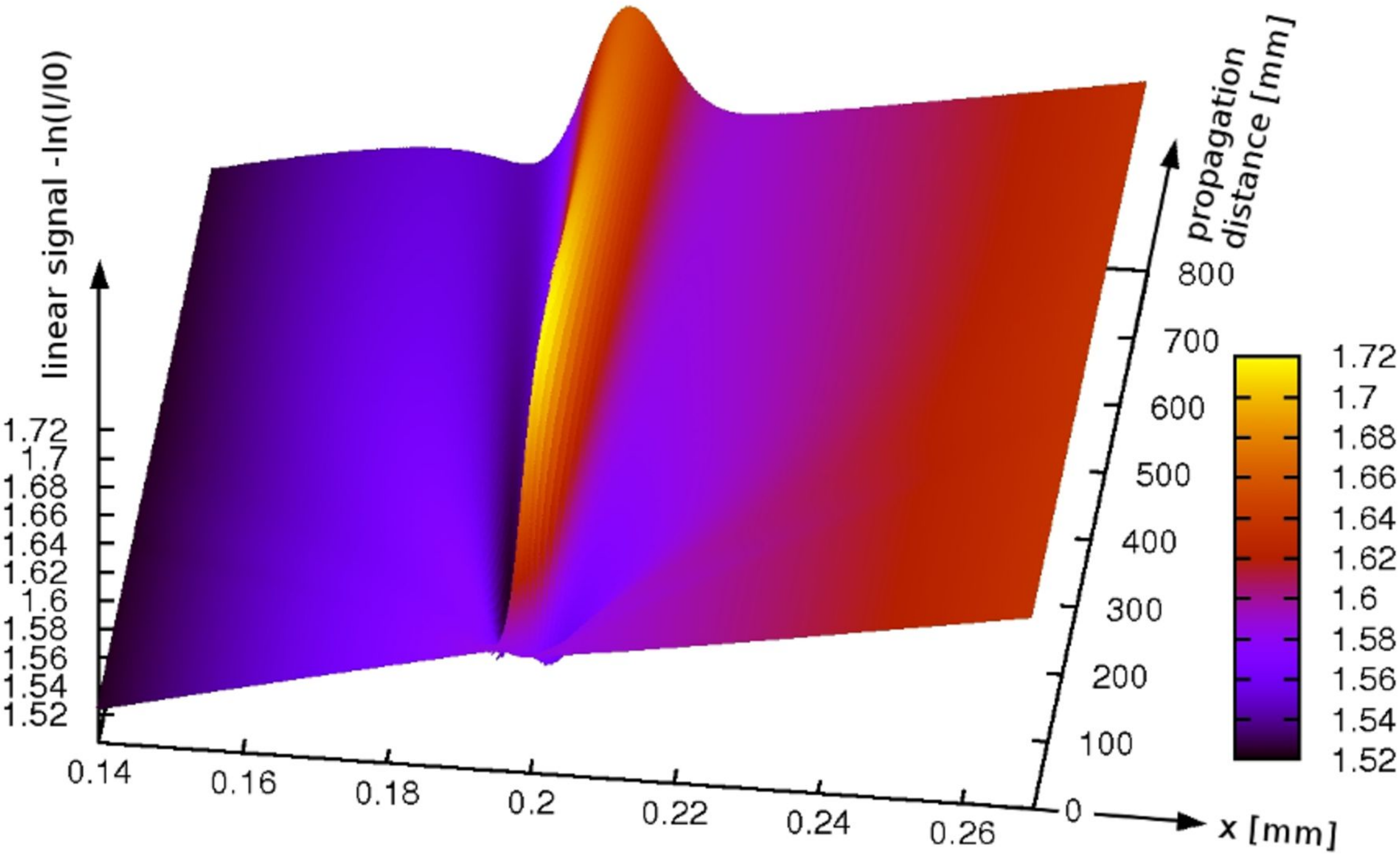
linear signal -ln(I/I0)
1.72
1.7
1.68
1.66
1.64
1.62
1.6
1.58
1.56
1.54
1.52
0.14
0.16
0.18
0.2
0.22
0.24
0.26
propagation distance [mm]
800
700
600
500
400
300
200
100
0
x [mm]
1.72
1.7
1.68
1.66
1.64
1.62
1.6
1.58
1.56
1.54
1.52

(b)

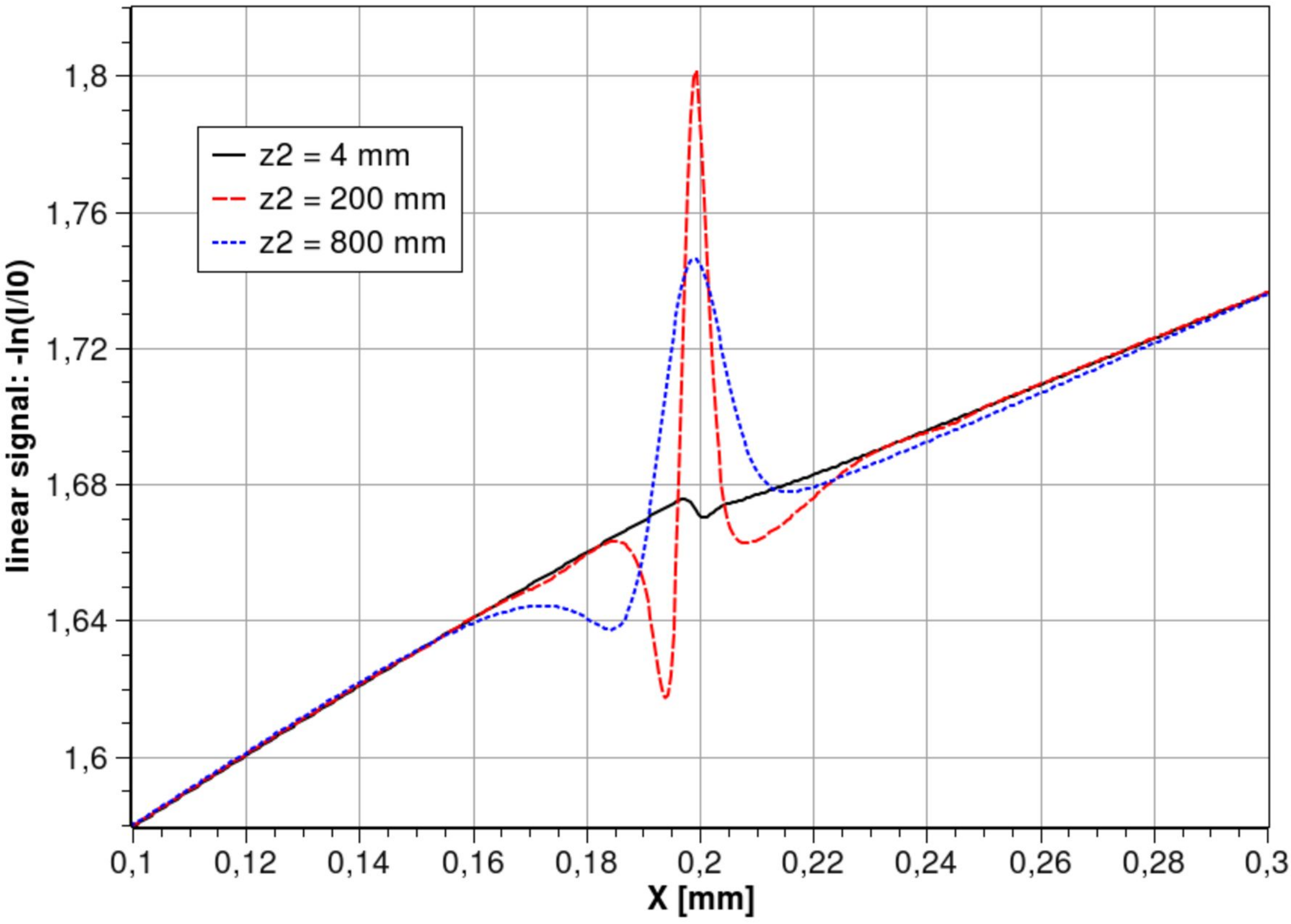
z2 = 4 mm
z2 = 200 mm
z2 = 800 mm
linear signal: -ln(I/I0)
1,8
1,76
1,72
1,68
1,64
1,6
0,1
0,12
0,14
0,16
0,18
0,2
0,22
0,24
0,26
0,28
0,3
X [mm]

(a)

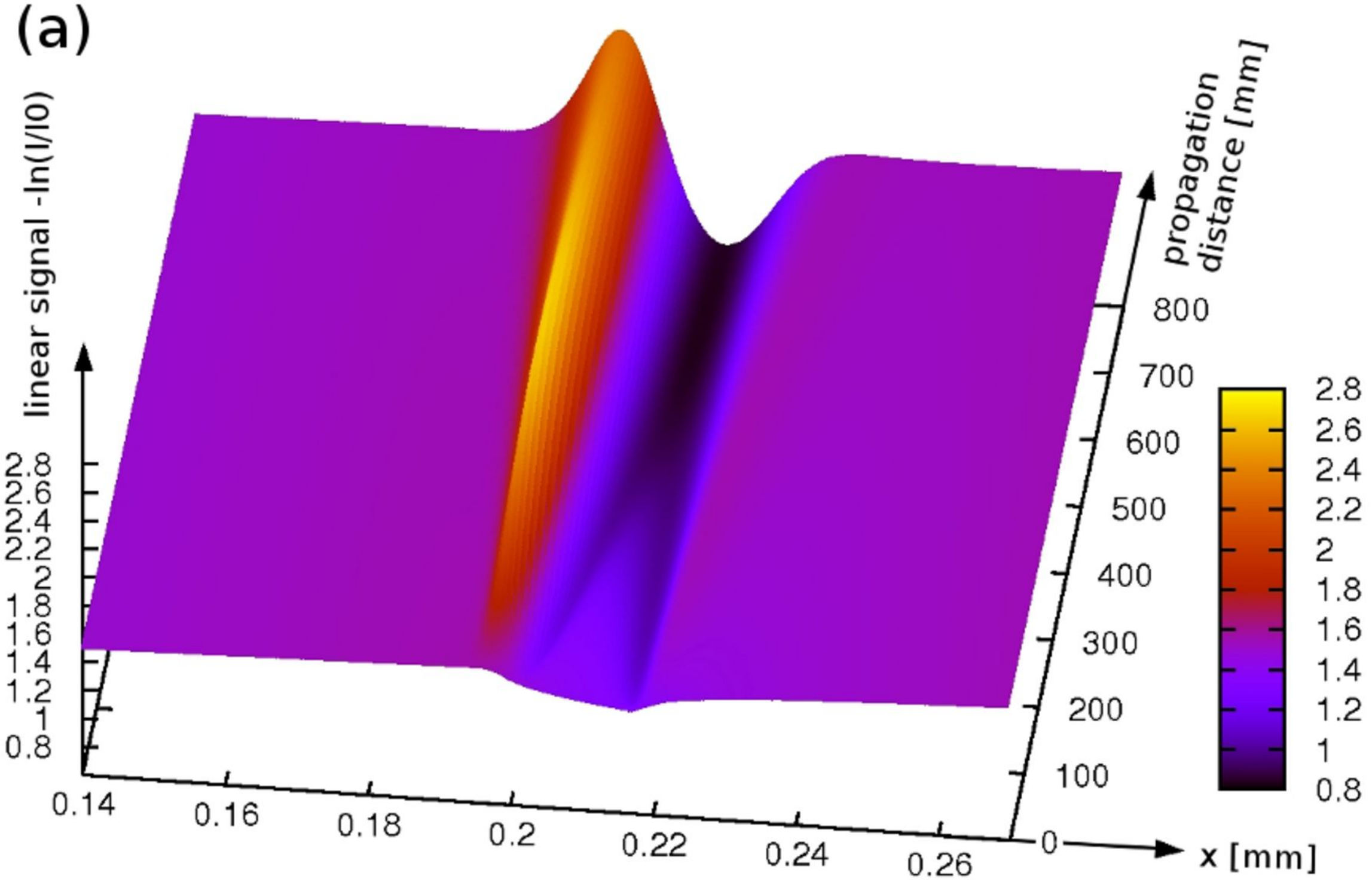
linear signal -ln(I/I0)
2.8
2.6
2.4
2.2
2
1.8
1.6
1.4
1.2
1
0.8
0.14
0.16
0.18
0.2
0.22
0.24
0.26
propagation distance [mm]
800
700
600
500
400
300
200
100
0
x [mm]

(b)

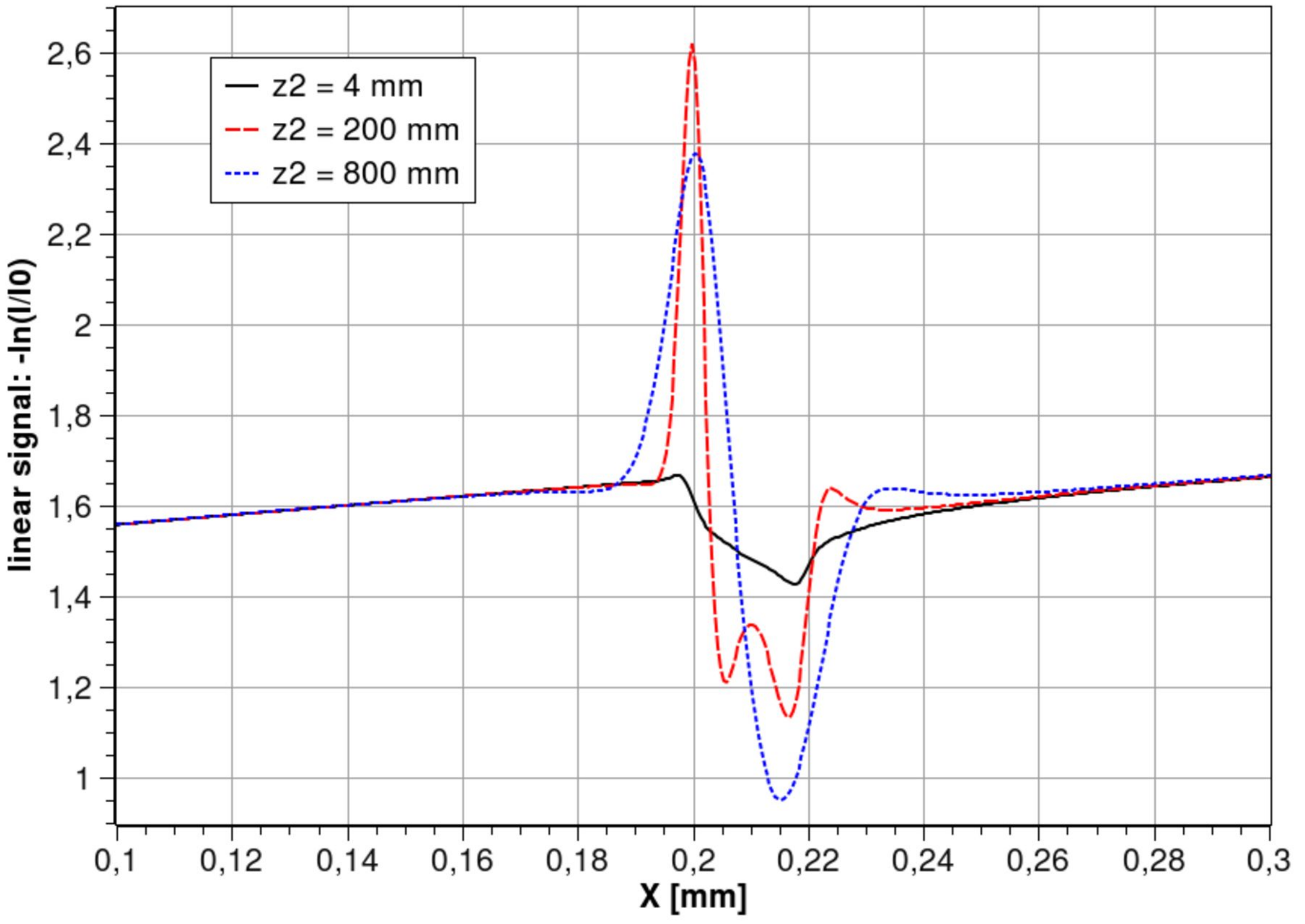
z2 = 4 mm
z2 = 200 mm
z2 = 800 mm
linear signal: -ln(I/I0)
2,6
2,4
2,2
2
1,8
1,6
1,4
1,2
1
0,1
0,12
0,14
0,16
0,18
0,2
0,22
0,24
0,26
0,28
0,3
X [mm]

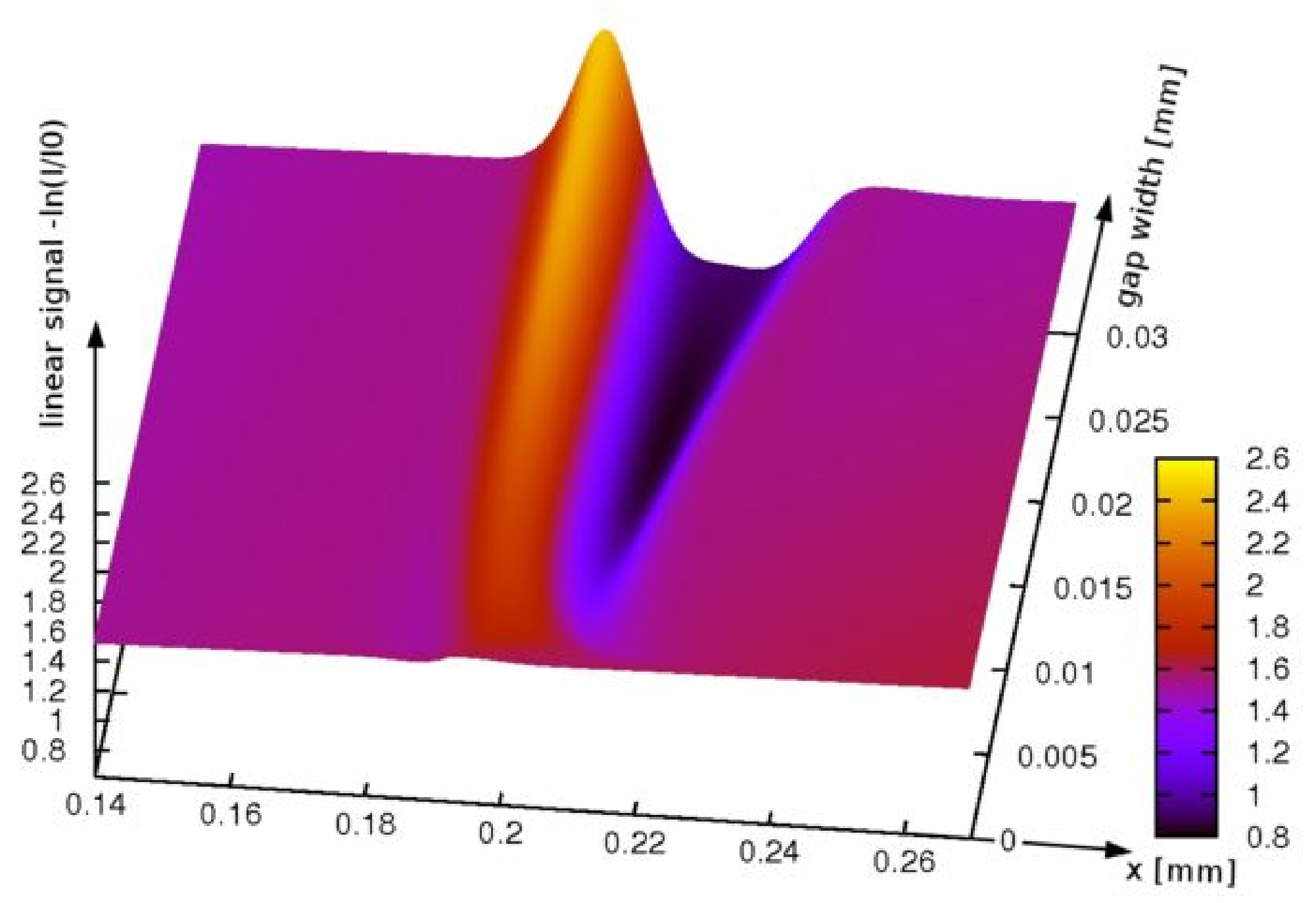
linear signal -ln(I/I0)
2.6
2.4
2.2
2
1.8
1.6
1.4
1.2
1
0.8
0.14
0.16
0.18
0.2
0.22
0.24
0.26
x [mm]
gap width [mm]
0.03
0.025
0.02
0.015
0.01
0.005
0
2.6
2.4
2.2
2
1.8
1.6
1.4
1.2
1
0.8

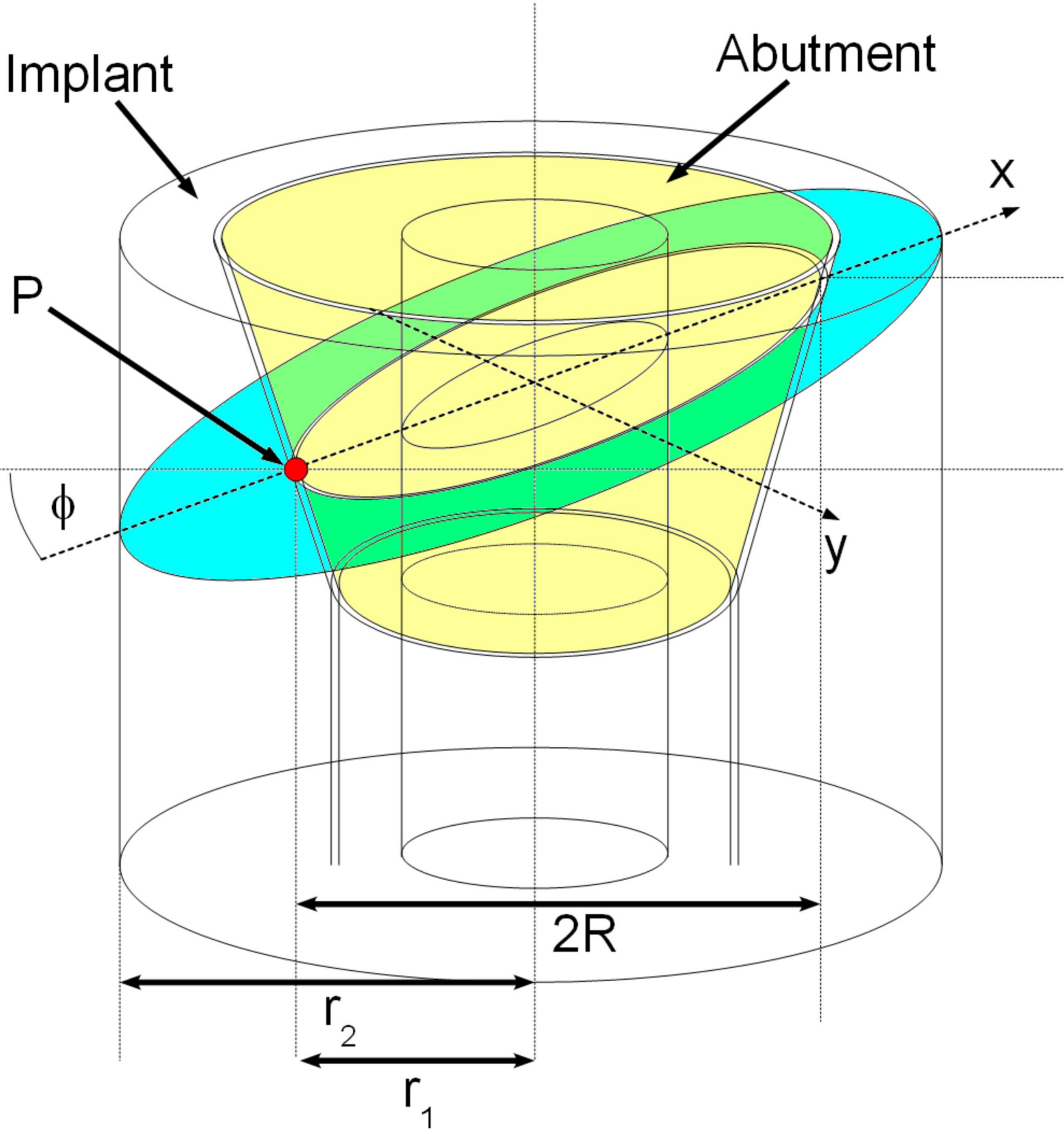
Implant
Abutment
X
P
ϕ
y
2R
r2
r1

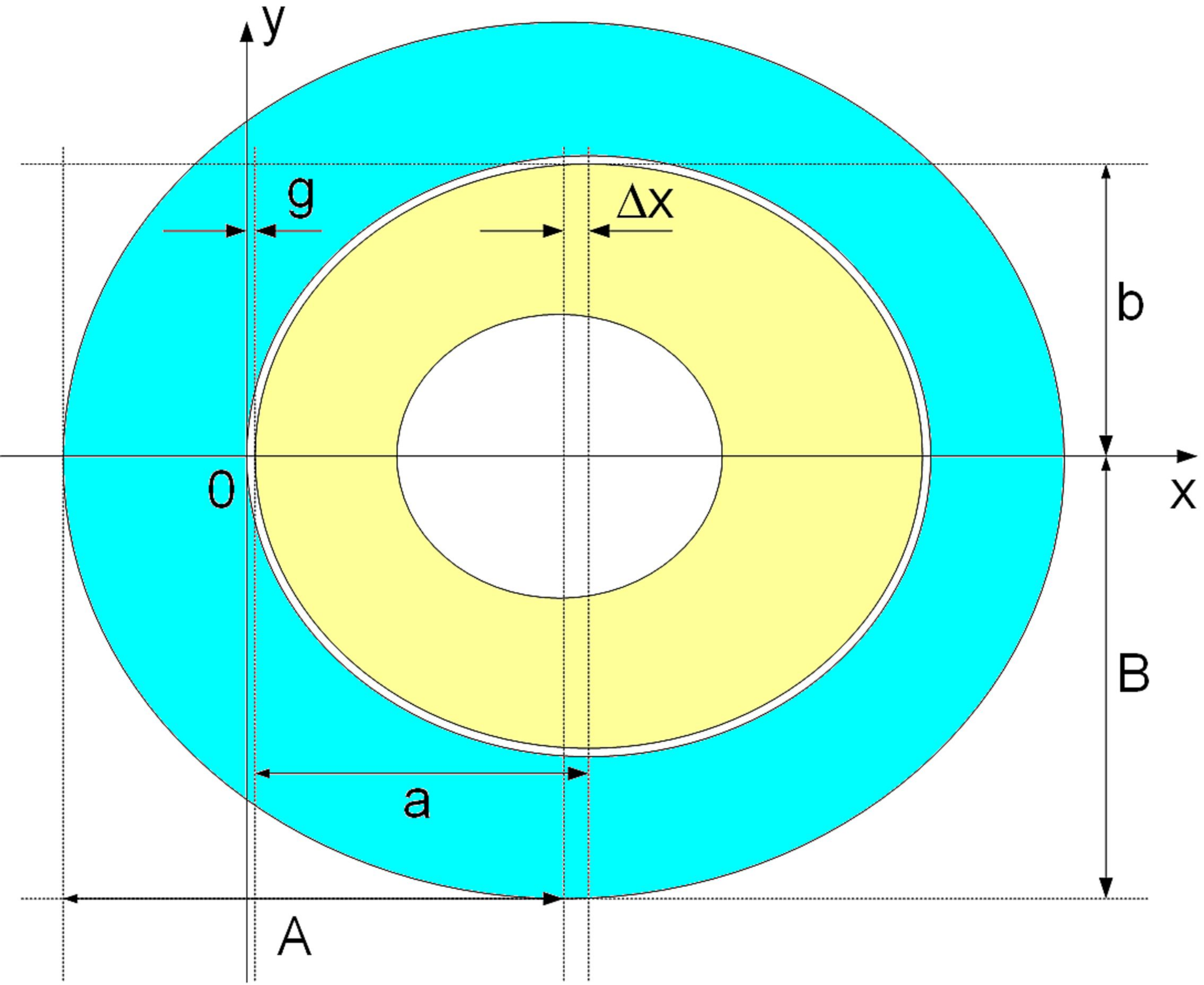
y
g
Δx
b
0
x
a
B
A